Monte Carlo studies of noncollinear magnetic phases in multiferroic Cu_2OSeO_3

Houssam Sabri* and Igor Kornev
Université Paris-Saclay, CentraleSupélec, CNRS, Laboratoire SPMS UMR 8580, 91190 Gif-sur-Yvette, France

(Received 30 September 2022; revised 6 November 2022; accepted 9 January 2023; published 17 January 2023)

Monte Carlo simulations based on a first-principles-derived Hamiltonian are conducted to study the finite-temperature properties of chiral-lattice multiferroic insulator Cu_2OSeO_3. The use of this numerical technique (i) reveals basic features of the phase diagram as a function of temperature and external magnetic field, including the long-range helical phase at low temperature and zero magnetic field and the skyrmion lattice phase, in which skyrmions are arranged in a two-dimensional hexagonal lattice, and (ii) leads to the discovery of an overlooked vortex lattice phase in a narrow pocket of the phase diagram near the fluctuations' disordered-helical phase transition. The scheme also provides strong numerical evidence that the transition to a helical state in Cu_2OSeO_3 is of first order driven by critical fluctuations.

DOI: 10.1103/PhysRevB.107.024417

I. INTRODUCTION

In recent years, there has been a surge in interest in topological spin textures due to their potential role as a building block in new spintronic devices [1]. A direct result of their topological stability is their robustness against continuous mechanical deformations and defects. An example of topological spin textures is skyrmions, which first emerged as a solution of the nonlinear field in the context of dense nuclear matter [2]. They are characterized by a topological invariant, which describes the local configuration of how the vector field whirls in the plan. This topological invariant categorizes the equivalent spin configurations in the case of magnetic systems [3]. The magnetic skyrmions were predicted to exist within magnets with relevant Dzyalonshinskii-Moriya interaction (DMI) [4,5]. They were first discovered in the noncentrosymmetric cubic B20 metallic chiral magnet MnSi [6], in other B20 crystals as FeGe [7], $Fe_{1-x}Co_xSi$ [8] both in bulk material and thin films [9], and also in other material with noncentrosymmetric crystal structures like β-Mn type Co-Zn-Mn alloys [10]. These topologically nontrivial spin configurations called skyrmions can be described as circular spin textures with spin up on the edge of the circle and spin down in the center. There is in between a smooth transition with topological features. Others such as copper oxide selenite Cu_2OSeO_3 that crystallize in the cubic space group $P2_13$ exhibit the same features of the B20 magnets [11]. However, this crystal is the only insulator in this family of chiral magnets that displays a multiferroic behavior with a magnetoelectric coupling [12,13]; this may give rise to the ferroelectric counterpart topological solitons and also the manipulation of skyrmions with an electric field [14].

The skyrmion lattice phase (SkL), in which the skyrmions are arranged in a two-dimensional hexagonal lattice, exists in a narrow pocket of magnetic field and temperature phase diagram near the paramagnetic-helical state phase transition temperature T_c. The helical state phase in Cu_2OSeO_3 is known to exist in a more extensive range of temperature-field (T-B) phase diagram [15]. The helical phase corresponds to a noncollinear magnetization pattern, in which spins are arranged in a periodic spiral. The helical phase arises from the competition between the collinear Heisenberg interaction and the noncollinear DMI. In the presence of Zeeman interaction, this competition may create in some conditions multiple helimagnetic states that overlap and create other spin textures like vortex lattices found recently in a centrosymmetric magnet $GdRu_2Si_2$ [16], hedgehog lattices, or skyrmion lattices [17]. The SkL is considered as the overlapping of three different helices with noncollinear and coplanar directions. The further contributions of thermal fluctuations stabilize the SkL and the ratio of Heisenberg exchange and DMI can determine the lattice constant of SkL and the size of skyrmions. The strength of both interactions does not depend on temperature; thus skyrmions' size and lattice constant are uniform on the whole lattice.

In the past years, there have been few attempts to model the behavior of Cu_2OSeO_3 with atomistic approaches. Janson *et al.* [18] attempted to reproduce the phase diagram with micromagnetic simulations which are fundamentally constrained by the continuum formulation [19,20]. Belemuk *et al.* [21] used artificial effective Hamiltonian parameters to model the high-pressure behavior of the phase transition in helical magnets. In this work, we investigate the helical phase and the SkL using the effective Hamiltonian method, which is parametrized using *ab initio* density functional theory (DFT) calculations. The resulting effective Hamiltonian is solved with Monte Carlo simulations. This approach is a purely atomistic attempt to reproduce the experimental phase diagram and gives us insight into the microscopic mechanism of creation and stability of the different magnetic phases and spin textures in multiferroic Cu_2OSeO_3.

II. EFFECTIVE HAMILTONIAN

The system's equilibrium properties at finite temperatures can be determined from the total energy, which is a function

*houssam.sabri@centralesupelec.fr

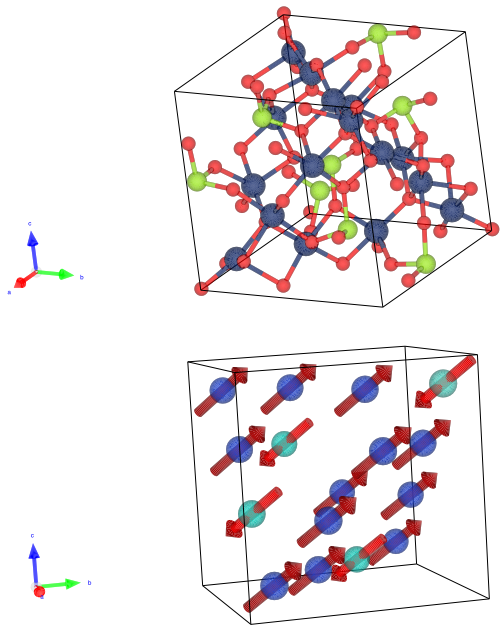

FIG. 1. Crystal structure of copper oxide selenite Cu_2OSeO_3: dark blue for copper, red for oxygen, and green for selenium. Magnetic atoms in the system: light blue for copper atoms I (Cu^I) and dark blue for copper atoms II (Cu^{II}).

of the atomic spins. The aim here is to build a parametrized Hamiltonian, which is totally *ab initio* with no experimental or empirical inputs.

The first term in our magnetic effective Hamiltonian is the Heisenberg interaction

$$E^H(\{\mathbf{S}\}) = \sum_{i<j} J_{ij}\mathbf{S}_i \cdot \mathbf{S}_j. \tag{1}$$

$E^H(\{\mathbf{S}\})$ is the energy contribution of collinear magnetic interaction at the atomic level. This interaction, in general, tends to make the spins align in the same direction [either ferromagnetic (FM) or antiferromagnetic (AF)]; in the case of the multiferroic Cu_2OSeO_3, the localized spin $S = \frac{1}{2}$ originates from the unpaired electron in the $3d$ shell and the copper ions Cu^{2+} make a network of tetrahedra made of four ions at each corner with two sites Cu^I and Cu^{II} with a ratio of $1:3$, as shown in Fig. 1. This network of copper ions and tetrahedra gives rise to five types of Heisenberg exchanges, each related to a type of interaction:

$$E^H(\{\mathbf{S}\}) = \sum_{i<j}\big[J_w^{FM}\mathbf{S}_i^{II}\cdot\mathbf{S}_j^{II} + J_s^{AF}\mathbf{S}_i^{I}\cdot\mathbf{S}_j^{II} + J_s^{FM}\mathbf{S}_i^{II}\cdot\mathbf{S}_j^{II} + J_w^{AF}\mathbf{S}_i^{I}\cdot\mathbf{S}_j^{II} + J_O^{AF}\mathbf{S}_i^{I}\cdot\mathbf{S}_j^{II}\big]. \tag{2}$$

J_w^{FM} (J_s^{FM}) is the weak (strong) ferromagnetic interaction between copper (Cu^{II}) atoms, J_s^{AF} (J_w^{AF}) is the strong antiferromagnetic interaction (weak) between copper (Cu^{II} and Cu^I) atoms, and J_O^{AF} is the only superexchange interaction (long-range coupling mediated by the bridging oxo ligand) that is comparable to previous ones.

The second term, which is a crucial ingredient in observing the noncollinear spin textures in magnetic materials, is the DMI, which is the antisymmetric exchange that prevents the spins from aligning in the same direction; this interaction arises from spin-orbit coupling and is written as

$$E^{DMI}(\{\mathbf{S}\}) = \sum_{i<j}\mathbf{D}_{ij}\cdot\mathbf{S}_i\times\mathbf{S}_j. \tag{3}$$

The same analysis goes for DMI, where we have five different vectors related to the Heisenberg exchange constant. These vectors give rise to the noncollinear magnetic textures (such as helical, conical, and skyrmion lattice states):

$$E^{DMI}(\{\mathbf{S}\}) = \sum_{i<j}\big[\mathbf{D}_w^{FM}\cdot\mathbf{S}_i^{II}\times\mathbf{S}_j^{II} + \mathbf{D}_s^{AF}\cdot\mathbf{S}_i^{I}\times\mathbf{S}_j^{II} + \mathbf{D}_s^{FM}\cdot\mathbf{S}_i^{II}\times\mathbf{S}_j^{II} + \mathbf{D}_w^{AF}\cdot\mathbf{S}_i^{I}\times\mathbf{S}_j^{II} + \mathbf{D}_O^{AF}\cdot\mathbf{S}_i^{I}\times\mathbf{S}_j^{II}\big]. \tag{4}$$

The last term is the Zeeman energy that describes the potential energy of the interaction between the spins and the applied external magnetic field $\mathbf{B}_{\text{ext}}$,

$$E^{\text{Zeeman}}(\{\mathbf{S}\}) = \sum_i g_S\frac{\mu_B}{\hbar}\mathbf{S}_i\cdot\mathbf{B}_{\text{ext}}, \tag{5}$$

where g_S is the Landé g factor ($g_S = 2$) and μ_B is the Bohr magneton.

The total energy based on this Hamiltonian which includes all previous interactions is used as the energy to minimize in Monte Carlo simulations, in order to compute the finite temperature properties.

III. COMPUTATIONAL DETAILS

A. DFT calculations

The first-principles density functional theory calculations were performed using the Vienna Ab initio Simulation Package (VASP) [22] for geometrical structure optimization and to calculate the Heisenberg exchange, DMI constants with the four energies states method [23,24].

The electronic wave function adopts a plane-wave basis and the pseudopotentials adopt the projector augmented-wave method (PAW), with generalized gradient approximation of Perdew, Burke, and Ernzernhof (GGA-PBE) [25] used as the exchange-correlation functional. For $3d$ orbitals of Cu atoms, a GGA + U correction is used within Dudarev's formulation [26] to treat the strong correlation properties of $3d$ electrons with U (on-site Coulomb repulsion energy) and J (Hund exchange parameter) set, respectively, to 7.5 eV and 0.98 eV [27]; the spin-orbit coupling parameter was turned on for the case of DMI. The plane-wave cutoff energy is set to 520 eV. The sampling of the Brillouin zone is done using a $4\times4\times4$ Γ-centered k mesh with the Monkhorst-Pack scheme.

B. Monte Carlo simulations

For our system's study at finite temperatures, we have performed Monte Carlo simulations that compute the change in total energy as the configuration of spins' changes. We solve the effective Hamiltonian using the Monte Carlo simulations, which rely on the Metropolis-Hastings algorithm [28,29] inside an $L\times L\times L = N_L$ cubic supercell with periodic boundary conditions, where N_L designate the total

TABLE I. Microscopic magnetic model parameters from DFT four states energy-mapping calculations: the columns respectively designate the interaction type, the type of atoms involved, the involved atoms (ρ_i, ρ_j), distance between atoms, the Heisenberg exchange, DMI vector, and the ratio between DMI and Heisenberg exchange. The atomic positions for all involved atoms are listed in the Supplemental Material. J and $\mathbf{D}$ parameters are normalized with respect to the DFT obtained value $S = 0.73$.

Interactions	Atoms	(ρ_i, ρ_j)	$d_{ij} = \lvert r_i - r_j \rvert$ (Å)	J_{ij} (K)	$\mathbf{D}_{ij}$ (K)	$\delta = \frac{\lvert \mathbf{D}_{ij} \rvert}{\lvert J_{ij} \rvert}$
J_w^{FM}, $\mathbf{D}_w^{FM}$	Cu^{II}-Cu^{II}	(ρ_8, ρ_7)	3.011	−27.57	(−2.53, −3.85, 0.201)	0.167
J_s^{AF}, $\mathbf{D}_s^{AF}$	Cu^{I}-Cu^{II}	(ρ_{12}, ρ_6)	3.067	146.76	(−3.596, 13.88, 9.75)	0.118
J_s^{FM}, $\mathbf{D}_s^{FM}$	Cu^{II}-Cu^{II}	(ρ_1, ρ_8)	3.226	−60.00	(4.573, 8.15,4.473)	0.173
J_w^{AF}, $\mathbf{D}_w^{AF}$	Cu^{I}-Cu^{II}	(ρ_{12}, ρ_{13})	3.336	16.84	(−9.53, 8.06, 6.84)	0.845
J_O^{AF}, $\mathbf{D}_O^{AF}$	Cu^{I}-Cu^{II}	(ρ_{16}, ρ_3)	6.396	30.57	(−0.55, 4.26, −3.88)	0.189

number of magnetic unit cells and each magnetic unit cell contains 16 spins. In order to decrease computation time, GPU parallel programing is employed. The magnetic Hamiltonian includes only short-range interactions, so a parallel checkerboard type algorithm is used [30] (see the Supplemental Material [31]).

The trial moves in our case consist of updating the spin vector direction (constant norm), which changes the total energy. For $L = 84$, which corresponds to $N_a \sim 10^7$ atoms, each Monte Carlo sweep (MCS) takes about 0.93 s on our cluster workstation. The total number of MCS is chosen to be 5×10^7 for every temperature step, with half of these sweeps used for thermalization and the other half for extracting equilibrium properties. This process is done by decreasing the temperature in small steps (annealing) to get well-converged results.

IV. RESULTS AND DISCUSSION

The crucial parameters in forming magnetic textures such as helical structure and magnetic skyrmions in Cu_2OSeO_3 are the magnetic interactions. We evaluate the Heisenberg interaction and DMI using the four-state energy-mapping method [23,24]. The results reveal two energy scales for exchange constants; for both ferromagnetic and antiferromagnetic exchanges, there is weak and strong interaction and an important superexchange (long-range) antiferromagnetic compared to weak interactions. Table I presents all the values for the five different exchanges and the corresponding DMI vectors. We observe that the ratio of DMI over Heisenberg constant δ, which is usually smaller than 0.05 [5], is between 0.11 and 0.20 and an enormous ratio of 0.84 in the case of the weak antiferromagnetic exchange J_w^{AF}, $\mathbf{D}_w^{AF}$. The immense ratio reveals the existence of a very strong DMI in our system, which is a necessary condition in the creation of magnetic textures and, in particular, magnetic skyrmions. We have compared our results with Janson *et al.* [18] starting with the exchange constants; we report a difference between the Heisenberg exchange in this paper and their results. The ratios between the DMI and Heisenberg interaction were smaller than 0.10, except for the weak antiferromagnetic exchange, where it is at the order of 0.58. The small ratios could be the origin of the absence of noncollinear spin textures when using their results as input parameters of our effective Hamiltonian. We have also compared our results with a previous study by Yang *et al.* [32] and find them to be consistent.

We also show that, using Monte Carlo simulations and the previous constants as parameters of effective Hamiltonian, the existence of a helical state at zero field characterized with a propagation vector $||\mathbf{q_H}|| = 0.008$ (Å^{-1}), the helical state has a periodicity along $[1\bar{1}0]$ direction [11] with a wavelength $\lambda_H \simeq 78.4$ nm, and is shown to exist in all of the temperature range below $T_H \simeq 37.5$ K, which delimits the helical phase from the fluctuations disordered phase. This value is lower than the critical temperature $T_c \simeq 42.5$ of the ordered phase to the paramagnetic phase where its experimental value is $T_c^{\text{expt}} \simeq 58$ K [15]. The discrepancy between the reported critical temperature and experimental one is due to the use of lattice constant of paramagnetic phase as lattice parameter in the range of temperatures of the field polarized phase (helical and SkL), which correspond to a 2 GPa applied hydrostatic pressure on the crystal which affects the magnetic exchange constant $T_c(P) = T_c(0)(1 - P/P_c)$ [33]. To explore those noncollinear phases we calculated the spin structure factor $\mathbf{F}(\mathbf{q})$, which is defined as the Fourier transform of the spin distribution. Figure 2(a) shows the logarithm of spin structure factor for our system at 35 K, where we find two spots corresponding to $\mathbf{q_H}$ and $-\mathbf{q_H}$, while Fig. 2(b) shows the spatial distribution of the spins in helical phase in a (001) layer; this feature has been proven experimentally with the exception in the reported wavelength $\lambda_H^{\text{expt}} \simeq 61.6 \pm 4.5$ nm [15], which is due to the same argument as T_c.

We also report that, for the heat capacity, we have the same peak and shoulder feature near T_c found in experimental results in MnSi and Cu_2OSeO_3 [34]. Figure 3 shows the feature where the shoulder is toward high temperatures. We emphasize that this is the first atomistic study with the *ab initio* inputs that reproduce this behavior. Belemuk *et al.* [21] show the same features with Monte Carlo simulation but with artificial inputs for Heisenberg exchange and DMI in the effective magnetic Hamiltonian. The first peak (which is field dependent) around $T_H \simeq 37$ K for zero field is a characteristic of a first-order phase transition between the fluctuation-disordered regime (FD) and helical state, as was discovered experimentally by Chauhan *et al.* [35]. The second peak (the shoulder) at $T \simeq T_c \sim 42.5$ K delimits the FD region from the uncorrelated paramagnetic region. Janoscheck *et al.* [36] showed that the phase transition in a helimagnet of the B20 family (MnSi) displays a fluctuation-induced first-order phase transition that follows a Brazovskii mechanism [37]. To explore the induced first-order phase transition mechanism, we

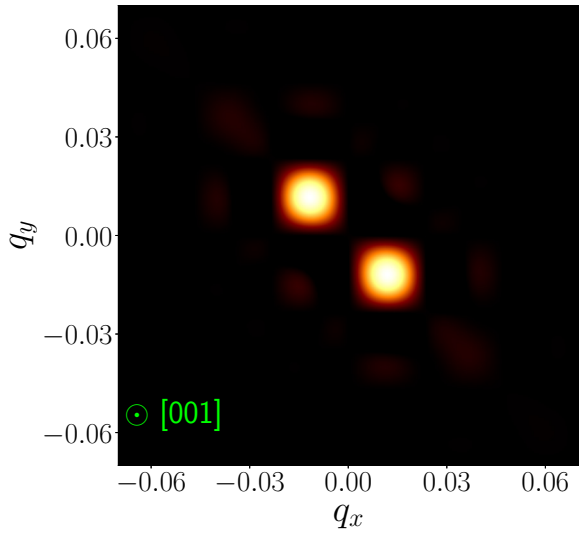

(a)

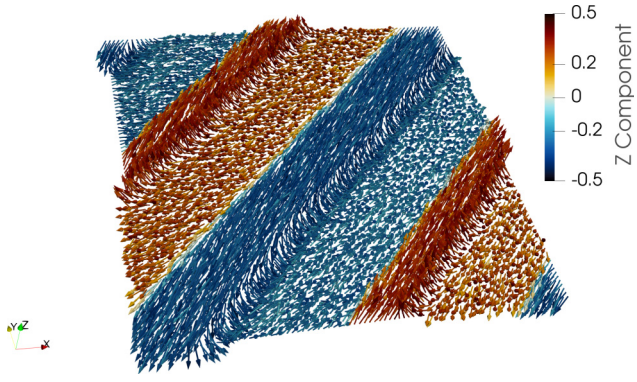

(b)

FIG. 2. (a) Logarithm of the square of spin structure factor $[\log_{10}(|\mathbf{F}|^2)]$, where $|\mathbf{F}|^2$ is summed along the [001] direction at 35 K and zero magnetic field, and (b) real space spin configuration in Cu_2OSeO_3 (001) slice in the helical phase. The z component and the in-plane orientations of the spins are illustrated by the color bar and colored arrows, respectively.

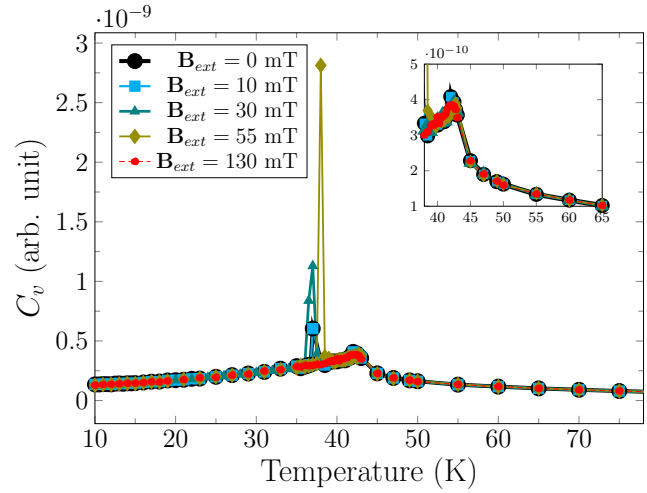

(a)

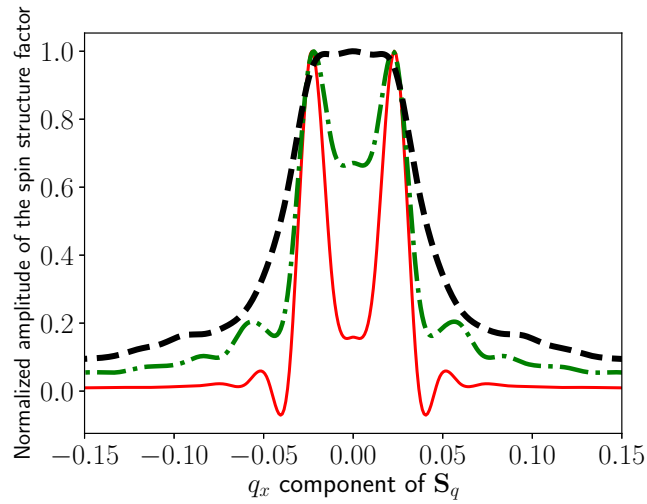

(b)

FIG. 3. (a) Heat capacity for multiple values of magnetic fields; the second-order phase transition is independent of magnetic fields, whereas the first-order phase transition is field dependent, where lines are guides to the eye. (b) The distribution of the spin Fourier component along $(1\bar{1}0)$ direction across the transition T_H: solid line is $T_H - 0.25$ K, dashed-dotted line is $T_H + 0.25$ K, and dashed line is $T_H + 2$ K. The transition from double peak distribution into single peak is a signature of first-order phase transition.

calculated the inverse of correlation length $\kappa = \frac{2\pi}{\xi}$ for temperature above T_H. There are several scenarios if the inverse Ginzburg length of the system κ_G satisfies the condition $\kappa_G < \kappa_{DM}$ for $T > T_H$, where $\kappa_{DM} = ||\mathbf{q}_H||$; the system undergoes a first-order transition that follows a Brazovskii mechanism. In this mechanism, the strongly interacting fluctuations suppress the mean-field transition temperature T_{MF}. On the other hand, if $\kappa_G > \kappa_{DM}$ the mechanism governing the induced phase transition can be described within the Wilson-Fisher renormalization group [38]. The latter mechanism is what governs the induced transition in Cu_2OSeO_3, as previously confirmed by Živković *et al.* [39]. The fit of the magnetic susceptibility with the Brazovskii Eq. (8) [36], where $\eta = \frac{\kappa_{Gi}}{\kappa_{DM}}$, gives a value of $\eta > 1$, which means that in our system $\kappa_G > \kappa_{DM}$,

$$\chi_{|T>T_c} = \frac{\chi_0}{1 + \eta^2 \mathcal{Z}(T)}, \tag{6}$$

$$\mathcal{Z}(T) = \frac{[\tau + (1 - \tau^3 + \sqrt{1 - 2\tau^3})^{1/3}]^2}{2^{1/3}[1 - \tau^3 + \sqrt{1 - 2\tau^3}]^{1/3}}, \tag{7}$$

$$\tau = \frac{T - T_{MF}}{T_0}. \tag{8}$$

Far from the transition, $T \gg T_c$, the fluctuations have a mean-field ferromagnetlike behavior as seen in Fig. 4(c). In our case, as the temperature approaches T_c from high temperatures, $\kappa < \kappa_G$, we enter the strongly interacting fluctuations regime that suppresses the transition temperature before the fluctuations' interactions acquire an isotropic chiral behavior. This can be seen from the spreading of propagation vectors in $\mathbf{q}$ space

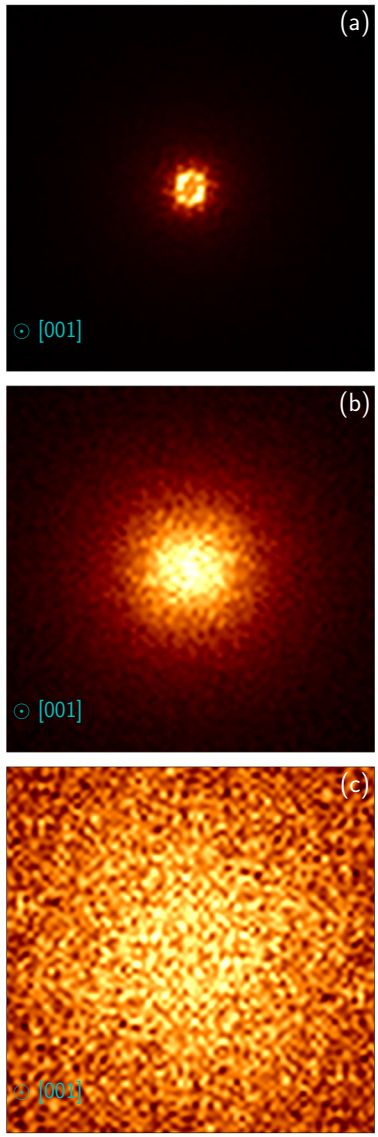

FIG. 4. Evolution of the spin structure factor in the first Brillouin zone (BZ) above T_c: (a) at $T_c + 0.5$ K, it shows isotropic chiral strongly interacting fluctuations, (b) the spreading of propagation vector on a sphere at $T_c + 3$ K, indicating strongly interacting fluctuations, and (c) at $T \gg T_c$ exhibiting ferromagnetic fluctuation behavior where the fluctuation spectrum spreads over the whole BZ.

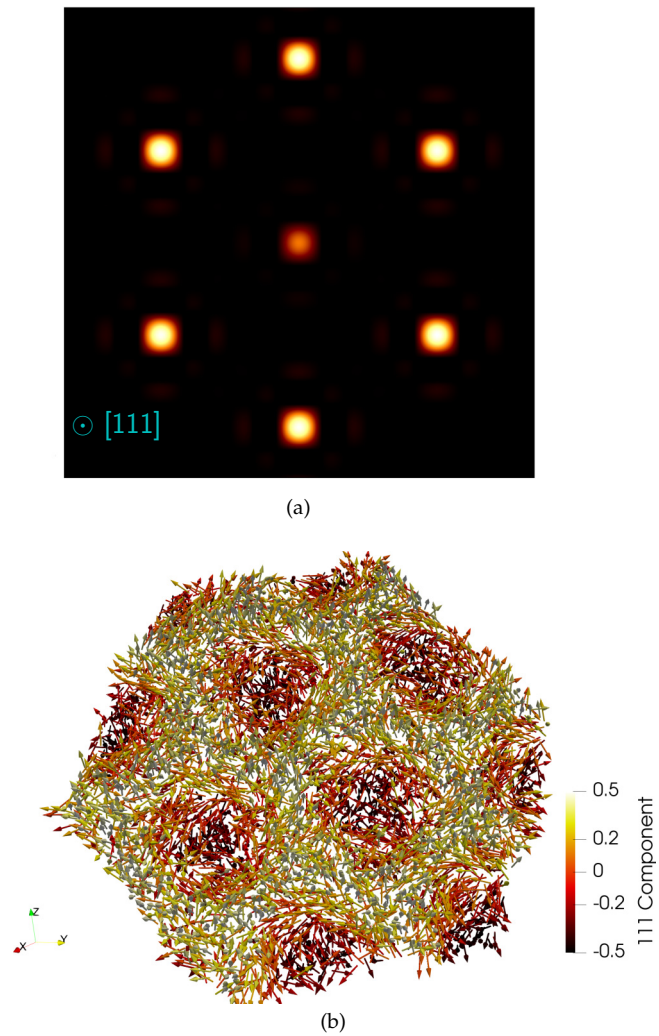

FIG. 5. (a) Logarithm of the square of the spin structure factor $[\log_{10}(|\mathbf{F}|^2)]$, where $|\mathbf{F}|^2$ is summed along the [111] direction at 35 K and 40 mT [111] magnetic field. Pixels on the corners of the image correspond to $|\mathbf{q}| \simeq 0.1$. (b) Real space spin configuration in Cu_2OSeO_3 (111) slice at the 35 K and 40 mT [111] magnetic field, which shows the skyrmion lattice. The z component and the in-plane orientations of the spins are illustrated by the color bar and colored arrows, respectively.

on a sphere as seen in Figs. 4(a) and 4(b). In this region, the inverse correlation length satisfies $\kappa \lesssim \kappa_{DM}$. However, these results remain indecisive since they rely on fitting the magnetic susceptibility with the Brazovskii equation to get the parameter η. Further study is required to directly extract the Ginzburg length and correlation length to fully understand the mechanism that induces the first-order phase transition.

The region between the helimagnetic transition and paramagnetic transition (between the first order and second order transition, $T_H < T < T_c$) is denoted as the fluctuation-disordered phase. In order to explore the nature of this phase, we study the evolution of the norm of the propagation vector as a function of temperature in the region $T_H < T < T_c$. We observe that the propagation vector related to the helical state is increasing in the norm, which indicates that the helical state periodicity is getting smaller to adapt to the supercell size, which in turn shows that the FD is an incommensurate phase. As the temperature increases, we observe spread over the Brillouin zone until we get a spherelike shape as in Fig. 4(a). The existence of an incommensurate phase along the FD phase, encapsulated by the commensurate phase (ferrimagnetic phase) and paramagnetic phase, indicates the existence of a Lifshitz point (LP) [40] at the border of these three phases.

Furthermore, in the case of an applied 40 mT magnetic field along (111) direction, we observe a skyrmion lattice phase in a range of temperature between 42.25 K and 34 K, which is characterized by three noncollinear propagation vectors: $\mathbf{q}^1_{\mathbf{SkL}} = \frac{1}{84}[\bar{2}11]$, $\mathbf{q}^2_{\mathbf{SkL}} = \frac{1}{84}[1\bar{2}1]$, and $\mathbf{q}^3_{\mathbf{SkL}} = \frac{1}{84}[11\bar{2}]$. Figure 5(a) shows the projection of the spin structure factor

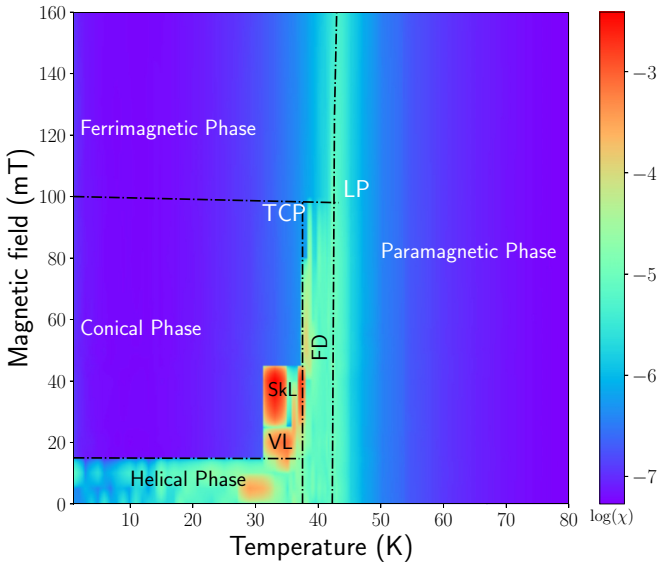

FIG. 6. Phase diagram of various magnetic orders in Cu_2OSeO_3: SkL, skyrmion lattice; VL, vortex lattice; FD, fluctuation disordered; TCP, tricritical point; LP, Lifshitz point. The logarithm of the magnetic susceptibility, the specific heat, and spin structure factor patterns at different temperatures and magnetic fields are used to calculate the borders of the phases.

in this case on the (111) plan, which shows a sixfold pattern, the six spots corresponding to $\mathbf{q}^{\mathbf{i}}_{\mathbf{SkL}}$ and $-\mathbf{q}^{\mathbf{i}}_{\mathbf{SkL}}$ with $i \in \{1, 2, 3\}$; these three noncollinear vectors are coplanar since $\det(\mathbf{q}^{\mathbf{1}}_{\mathbf{SkL}}, \mathbf{q}^{\mathbf{2}}_{\mathbf{SkL}}, \mathbf{q}^{\mathbf{3}}_{\mathbf{SkL}}) = 0$, which is a necessary condition for having a skyrmion lattice; otherwise, the three vectors would characterize a hedgehog lattice phase [41]. Figure 5(b) shows the skyrmions' lattice in real space.

To understand the mechanism of the creation of SkL, we performed a series of low magnetic field calculations, leading to the magnetic field-temperature phase diagram shown in Fig. 6 and, as predicted by the present scheme, seven phases exist within this range; five are well known, namely the helical, conical, SkL, paramagnetic, and ferrimagnetic (field polarised) phases. Moreover, we have two other phases; the first of them is between the helical phase and the SkL (at 15 mT), where a double noncollinear $\mathbf{q}$ pattern is created, indicating the existence of an intermediate vortex lattice (half skyrmions or merons). This prediction is yet to be confirmed experimentally. The last phase is previously mentioned where there is a dominance of fluctuation in the fluctuation-disordered regime. The phase diagram shows a tricritical point at the crossing between the conical, FD phase, and ferrimagnetic phase, as previously shown experimentally [35].

The vortex lattice phase is found to exist in a very tiny pocket near T_H, and between $\mathbf{B}_{\text{ext}}$ of stable helical phase and stable SkL, and has never been suggested as a possible ground state of Cu_2OSeO_3. The existence of the vortex lattice phase implies that the transition from helical state to SkL undergoes a step-by-step transition in terms of the topological invariant by passing from the topologically trivial single $\mathbf{q}$ state to a double $\mathbf{q}$ state characterized with a half-integer invariant to a triple $\mathbf{q}$ state with an integer invariant.

V. CONCLUSION

We have developed a first-principle approach to study the magnetic phases and finite-temperature properties of multiferroic chiral magnet copper oxide selenite Cu_2OSeO_3. We constructed an effective Hamiltonian with all the magnetic interactions; the parameters of this Hamiltonian were determined via density functional theory calculations with U correction (DFT + U). The Monte Carlo simulation gives us insight into the finite-temperature properties of Cu_2OSeO_3. We have obtained the same experimental head and shoulder peak signature of heat capacity found in Cu_2OSeO_3 and B20 magnets in general. We have found a very narrow pocket of temperature and magnetic field where the magnetic skyrmion lattice phase is stabilized in agreement with experimental observations and a stabilized magnetic helical phase at zero or small field under the critical temperature T_c. Our calculation also predicts the existence of a vortex lattice phase at a tiny region near T_H, between the helical phase and the SkL phase. This approach may be further enriched with the same ferroelectric Hamiltonian approach by Zhong, Vanderbilt, and Rabe [42] to study the multiferroic behavior of Cu_2OSeO_3, to understand the origin of magnetoelectric coupling, and also to study the topological defects in ferroic materials.

ACKNOWLEDGMENTS

The authors are grateful for support provided by NVIDIA via the NVIDIA GPU Grant. This work was performed using HPC resources from the Mésocentre" computing center of CentraleSupélec and École Normale Supérieure Paris-Saclay supported by CNRS and Région Île-de-France [43]. This project has received funding from the European Union's Horizon 2020 research and innovation programme under Grant Agreement No. 964931 (TSAR).

[1] W. Kang, Y. Huang, C. Zheng, W. Lv, N. Lei, Y. Zhang, X. Zhang, Y. Zhou, and W. Zhao, Voltage controlled magnetic skyrmion motion for racetrack memory, Sci. Rep. **6**, 23164 (2016).

[2] T. Skyrme, A unified field theory of mesons and baryons, Nucl. Phys. **31**, 556 (1962).

[3] S. Heinze, K. Von Bergmann, M. Menzel, J. Brede, A. Kubetzka, R. Wiesendanger, G. Bihlmayer, and S. Blugel, Spontaneous atomic-scale magnetic skyrmion lattice in two dimensions, Nat. Phys. **7**, 713 (2011).

[4] I. Dzyaloshinskii, A thermodynamic theory of "weak" ferromagnetism of antiferromagnetics, J. Phys. Chem. Solids **4**, 241 (1958).

[5] T. Moriya, Anisotropic superexchange interaction and weak ferromagnetism, Phys. Rev. **120**, 91 (1960).

[6] S. Muhlbauer, B. Binz, F. Jonietz, C. Pfleiderer, A. Rosch, A. Neubauer, R. Georgii, and P. Boni, Skyrmion lattice in a chiral magnet, Science **323**, 915 (2009).

[7] X. Yu, N. Kanazawa, Y. Onose, K. Kimoto, W. Zhang, S. Ishiwata, Y. Matsui, and Y. Tokura, Near room-temperature

formation of a skyrmion crystal in thin-films of the helimagnet FeGe, Nat. Mater. **10**, 106 (2011).

[8] W. Münzer, A. Neubauer, T. Adams, S. Muhlbauer, C. Franz, F. Jonietz, R. Georgii, P. Boni, B. Pedersen, M. Schmidt, A. Rosch, and C. Pfleiderer, Skyrmion lattice in the doped semiconductor $Fe_{1-x}Co_xSi$, Phys. Rev. B **81**, 041203(R) (2010).

[9] X. Yu, Y. Onose, N. Kanazawa, J. Park, J. Han, Y. Matsui, N. Nagaosa, and Y. Tokura, Real-space observation of a two-dimensional skyrmion crystal, Nature (London) **465**, 901 (2010).

[10] Y. Tokunaga, X. Yu, J. White, H. Rønnow, D. Morikawa, Y. Taguchi, and Y. Tokura, A new class of chiral materials hosting magnetic skyrmions beyond room temperature, Nat. Commun. **6**, 7638 (2015).

[11] S. Seki, X. Yu, S. Ishiwata, and Y. Tokura, Observation of Skyrmions in a Multiferroic Material, Science **336**, 198 (2012).

[12] J. Bos, C. Colin, and T. Palstra, Magnetoelectric coupling in the cubic ferrimagnet Cu_2OSeO_3, Phys. Rev. B **78**, 094416 (2008).

[13] E. Ruff, P. Lunkenheimer, A. Loidl, H. Berger, and S. Krohns, Magnetoelectric effects in the skyrmion host material Cu_2OSeO_3, Sci. Rep. **5**, 15025 (2015).

[14] J. White, I. Levatić, A. Omrani, N. Egetenmeyer, K. Prša, I. Živković, J. Gavilano, J. Kohlbrecher, M. Bartkowiak, H. Berger, and H. Rønnow, Electric field control of the skyrmion lattice in Cu_2OSeO_3, J. Phys.: Condens. Matter **24**, 432201 (2012).

[15] T. Adams, A. Chacon, M. Wagner, A. Bauer, G. Brandl, B. Pedersen, H. Berger, P. Lemmens, and C. Pfleiderer, Long-Wavelength Helimagnetic Order and Skyrmion Lattice Phase in Cu_2OSeO_3, Phys. Rev. Lett. **108**, 237204 (2012).

[16] N. Khanh, T. Nakajima, X. Yu, S. Gao, K. Shibata, M. Hirschberger, Y. Yamasaki, H. Sagayama, H. Nakao, L. Peng, K. Nakajima, R. Takagi, T. Arima, Y. Tokura, and S. Seki, Nanometric square skyrmion lattice in a centrosymmetric tetragonal magnet, Nat. Nanotechnol. **15**, 444 (2020).

[17] K. Shimizu, S. Okumura, Y. Kato, and Y. Motome, Phase transitions between helices, vortices, and hedgehogs driven by spatial anisotropy in chiral magnets, Phys. Rev. B **103**, 054427 (2021).

[18] O. Janson, I. Rousochatzakis, A. Tsirlin, M. Belesi, A. Leonov, U. Rößler, J. Brink, and H. Rosner, The quantum nature of skyrmions and half-skyrmions in Cu_2OSeO_3, Nat. Commun. **5**, 5376 (2014).

[19] R. Evans, *Atomistic Spin Dynamics*, Handbook of Materials Modeling: Applications: Current and Emerging Materials (Springer, New York, 2018), pp. 1–23.

[20] R. Evans, W. Fan, P. Chureemart, T. Ostler, M. Ellis, and R. Chantrell, Atomistic spin model simulations of magnetic nanomaterials, J. Phys.: Condens. Matter **26**, 103202 (2014).

[21] A. Belemuk and S. Stishov, Monte Carlo modeling the phase diagram of magnets with the Dzyaloshinskii-Moriya interaction, Solid State Commun. **267**, 6 (2017).

[22] G. Kresse and J. Furthmüller, Efficient iterative schemes for *ab initio* total-energy calculations using a plane-wave basis set, Phys. Rev. B **54**, 11169 (1996).

[23] H. Xiang, E. Kan, S. Wei, M. Whangbo, and X. Gong, Predicting the spin-lattice order of frustrated systems from first principles, Phys. Rev. B **84**, 224429 (2011).

[24] D. Šabani, C. Bacaksiz, and M. Milosevic, *Ab initio* methodology for magnetic exchange parameters: Generic four-state energy mapping onto a Heisenberg spin Hamiltonian, Phys. Rev. B **102**, 014457 (2020).

[25] J. Perdew, K. Burke, and M. Ernzerhof, Generalized Gradient Approximation Made Simple, Phys. Rev. Lett. **77**, 3865 (1996).

[26] S. Dudarev, G. Botton, S. Savrasov, C. Humphreys, and A. Sutton, Electron-energy-loss spectra and the structural stability of nickel oxide: An LSDA+U study, Phys. Rev. B **57**, 1505 (1998).

[27] V. Anisimov, J. Zaanen, and O. Andersen, Band theory and Mott insulators: Hubbard U instead of stoner I, Phys. Rev. B **44**, 943 (1991).

[28] N. Metropolis and S. Ulam, The Monte Carlo method, J. Am. Stat. Assoc. **44**, 335 (1949).

[29] W. Hastings, Monte Carlo sampling methods using Markov chains and their applications, Biometrika **57**, 97 (1970).

[30] T. Preis, P. Virnau, W. Paul, and J. Schneider, GPU accelerated Monte Carlo simulation of the 2D and 3D Ising model, J. Comput. Phys. **228**, 4468 (2009).

[31] See Supplemental Material at http://link.aps.org/supplemental/10.1103/PhysRevB.107.024417 for details on the parallel checkerboard algorithm.

[32] J. Yang, Z. Li, X. Lu, M. Whangbo, S. Wei, X. Gong, and H. Xiang, Strong Dzyaloshinskii-Moriya Interaction and Origin of Ferroelectricity in Cu_2SeO_3, Phys. Rev. Lett. **109**, 107203 (2012).

[33] P. Mohn, *Magnetism in the Solid State*, Solid-State Sciences (Springer-Verlag, Berlin, 2003).

[34] V. Sidorov, A. Petrova, P. Berdonosov, V. Dolgikh, and S. Stishov, Comparative study of helimagnets MnSi and Cu_2OSeO_3 at high pressures, Phys. Rev. B **89**, 100403 (2014).

[35] H. Chauhan, B. Kumar, J. Tiwari, and S. Ghosh, Multiple phases with a tricritical point and a Lifshitz point in the skyrmion host Cu_2OSeO_3, Phys. Rev. B **100**, 165143 (2019).

[36] M. Janoschek, M. Garst, A. Bauer, P. Krautscheid, R. Georgii, P. Böni, and C. Pfleiderer, Fluctuation-induced first-order phase transition in Dzyaloshinskii-Moriya helimagnets, Phys. Rev. B **87**, 134407 (2013).

[37] S. Brazovskĭ, Phase transition of an isotropic system to a nonuniform state, Sov. JETP **41**, 85 (1975).

[38] K. Wilson, The renormalization group and critical phenomena, Rev. Mod. Phys. **55**, 583 (1983).

[39] I. Živković, J. S. White, H. M. Rønnow, K. Prsa, and H. Berger, Critical scaling in the cubic helimagnet Cu_2OSeO_3, Phys. Rev. B **89**, 060401(R) (2014).

[40] R. Hornreich, M. Luban, and S. Shtrikman, Critical Behavior at the Onset of $\vec{k}$-Space Instability on the λ Line, Phys. Rev. Lett. **35**, 1678 (1975).

[41] N. Kanazawa, S. Seki, and Y. Tokura, Noncentrosymmetric magnets hosting magnetic skyrmions, Adv. Mater. **29**, 1603227 (2017).

[42] W. Zhong, D. Vanderbilt, and K. Rabe, First-principles theory of ferroelectric phase transitions for perovskites: The case of $BaTiO_3$, Phys. Rev. B **52**, 6301 (1995).

[43] http://mesocentre.centralesupelec.fr/.